5.4.4 The Post-Flare Phase

A new phase of flare activity, namely a late, high-altitude, coronal phase, was first identified in SMM data for May 21/22 by Svestka *et al.* (1982a). Other similar events from SMM were reported by Lantos *et al.* (1982) and Svestka *et al.* (1982b and c), and in retrospect some of the large-scale structures observed by Webb and Kundu (1978) probably fall in this category.

Based upon HXIS observations, Svestka (private communication) has estimated that the total energy content of the post-flare arch structures in the 21 May event was between 1.5×10^{29} and 4.7×10^{30} ergs; the total energy in the analogous structure of the November 6 event was 1.2×10^{31} ergs. In both cases, the estimated energies are comparable to the energies of other major flare components. It is necessary in a complete picture of flare energetics to understand the relationship between these manifestations and those of the more well-known flare phases. It is premature, based upon the limited number of events — not all of which may be of the same type — to draw general conclusions yet.

5.4.5 Phenomena in the Distant Corona

Coronal transients, coronal mass ejections, interplanetary shock waves, and the like have an uncertain but important place in flare energetics. These phenomena can be observed by coronagraphs and by meter-wave radio telescopes, as well as by *in situ* techniques at larger distances from the Sun. The Skylab coronagraph observations provided the earliest comprehensive views of coronal transients (Rust *et al.*, 1980), and observations have continued both in space (SMM and P78-1) and on the ground (notably with the Mauna Loa K-coronameter).

The relationship of these coronal phenomena with classical Hα "chromospheric flares," or with the high-energy flare events, remains problematical. There is no doubt that major flares often produce major coronal transients, but we have to guard against inferring a causal relationship: the BFS may confuse the picture (Kahler 1982). Indeed the suggested existence of "forerunner" coronal transients (Jackson and Hildner 1978) could imply that the coronal phenomena cause the flare rather than the other way round, and this is consistent with some theoretical views. The relationships are obscured by two major factors: there are only limited quantitative observations in the key inner corona, and in the outer corona there is confusion and uncertainty in the assignment of a given event to a given flare because of overlapping in time. Finally, it is known that coronal transients, especially with low speeds, may arise without the occurrence of a flare (Wagner, 1984). These events tend to fall in the "eruptive prominence" classification.

The energetics analysis of coronal phenomena has not advanced appreciably since the Skylab Workshop treatment (Webb *et al.*, 1980). Among the prime flares studied by the energetics team in this chapter, only one (June 29) had C/P observations. However, even this limb flare was not satisfactory for quantitative energetics analysis because it could not properly be compared with the disk flares in the remainder of our list.

5.5 CHARACTERIZATION OF TOTAL FLARE ENERGY

H.S. Hudson

5.5.1 Statement of the Problem

5.5.1.1 Introduction

The total energy released by a solar flare has a certain distribution in form as well as a certain pattern of flow among the several forms, as described above. As data have grown more comprehensive, the definition of this distribution has improved; classical assessments are found in the works of Ellison (1963), Bruzek (1967), Smith and Smith (1963), and Smith and Gottlieb (1975). Most recently the Skylab flare workshop (Sturrock 1980) addressed this question in two surveys of a single well-observed flare on 1973 September 5. These surveys dealt with the radiant energy (Canfield *et al.*, 1980) and the mechanical energy (Webb *et al.*, 1980), and their results have become the definitive data on flare energetics despite acknowledged gaps in coverage and in theoretical understanding.

This section aims at updating our knowledge of this fundamental matter. Unfortunately, there are still limitations in data coverage, as described in detail below. In some areas, notably the X-ray and gamma-ray ranges, there have been striking improvements, as reported above. We summarize the improvements here and take the further step of attempting to fill in the gaps in coverage to estimate the total radiant energy. One purpose for doing this is to permit a comparison of the observed or estimated total with the upper limits derived from the precise total-irradiance monitor (the Active Cavity Radiometer Irradiance Monitor-ACRIM) on SMM.

5.5.1.2 Availability of Data

What are the key limitations in the data set available to us? The foregoing discussions have naturally emphasized the observed forms and have relied on theoretical considerations to bridge the gaps. Where are the largest gaps? We discuss these items briefly here and present recommendations for future observations in Section 5.6.

The most important omissions from the data set fall into two major areas: the radiant energy in optical and EUV wavelengths, and coronal observations of all types. The brightness of the quiet Sun makes the optical wavelengths

particularly important, since an undetectably small optical continuum (for example) could rival the energy in wavelength ranges for which flares produce greater contrast. The Sacramento Peak observations from the white-light flare patrol show that continuum emission is not the rarity once thought (Neidig and Cliver 1984), and the line emission spectrum may contain even more energy. Even where spectrographic observations exist, these usually have covered only a fraction of the flare area or time profile, so that no definitive knowledge of the distributions even in a statistical sense now exists.

At EUV and XUV wavelengths a similar lack of coverage is striking; even though SMM carried an EUV instrument, its observations were extremely limited in coverage by a lack of imaging capability and appropriate telemetry bandwidth. SMM did not carry an XUV instrument, and so this vital wavelength range was totally omitted from consideration either from the diagnostic or the energetic point of view. Finally, considerable flare energy could appear at infrared wavelengths, but because of the simplicity of the emission mechanisms (H and H-free-free and free-bound continua should dominate), the omission of direct observations is less important than that of the optical and EUV-XUV ranges.

The optical and EUV-XUV data provide us with our best knowledge of the magnetic field distribution. Although vector-magnetograph observations began in a systematic way during the past solar maximum (Hagyard 1984), data that are extensive, precise, and sensitive enough to characterize the field adequately do not exist. As a result, we have only rough knowledge of the system of currents flowing in and around a flaring active region.

More serious omissions occurred in the area of coronal observations. The existing coronal observations have neither the sensitivity nor the diagnostic capability to contribute effectively to determining the key physical conditions in the corona. This is an enormous loss, because the coronal aspects of solar flares (at least in some cases, such as that of the well-documented Skylab flare of 1973 September 5) may dominate the total energy. In addition, the white-light coronagraph on board the SMM provided observations of only one of the well-observed prime flares chosen for detailed study here.

Because of these problems in availability of coronal data, this report does not address the non-radiant energy of a solar flare. This problem is reserved for a future solar maximum.

5.5.2 Techniques for Estimating Radiant Energy

5.5.2.1 Direct Observation

The radiant energy would ideally be determined from a full knowledge of the specific intensity as a function of wavelength, position, and time. Unfortunately, we must deal with integrals or small samples of this abstract function. Since our goal is to define the integral radiant energy in broad wavelength bands, fully detailed spectral information is important only for diagnostic purposes. At the highest energies, the coverage from broad-band soft and hard X-ray and gamma-ray detectors adequately describes the total flare radiation. The very large contrast of flare radiation at these wavelengths makes background subtraction, even for the disk-integrated radiation, relatively simple.

5.5.2.2 Differential Emission Measure (DEM)

Although observations are rarely available for wavelengths longer than about 20 Å, there is generally sufficient diagnostic information to characterize a DEM, as described in Section 5.3.2.1. With such a tool one can turn to a tabulation of the characteristic radiations for a plasma of the proper temperatures and, with assumptions about plasma conditions (abundances and state of equilibrium), estimate the total theoretical luminosity. Cox and Tucker (1969) provided one of the first systematic tabulations of characteristic plasma radiations.

The DEM approach works well enough for the present application at temperatures above a few million Kelvin, and this technique provides a much better characterization of the X-ray emission from flares than was previously possible. Unfortunately, the missing wavelength ranges contain emission lines necessary to define the temperature domain from a few million Kelvin down through the transition region, and so this domain requires an extrapolation to obtain complete coverage.

5.5.2.3 Scaling

For the lowest temperatures, including those responsible for the dominant optical-EUV-XUV radiations, the DEM approach cannot work in principle because the fundamental assumption of this techinique, i.e., that the strong resonance lines (and possibly the continuum) are optically thin, is incorrect. For these wavelengths, the only possible route to obtaining energy estimates is through scaling from a well-observed representative wavelength such as Hα. Unfortunately, even the Hα line seldom is observed with simultaneous line profile and imaging data, so that it cannot be used as a reference; furthermore, no detailed studies of the errors induced by the scaling approach exist. Is the rest of the Balmer series inferrable from the Hα line alone? Is the line-to-continuum ratio approximately a constant from flare to flare, or across the space or time profiles of a given flare? Is the scaling approach adequate for regions of different morphological class — for example "broad line" and "narrow line" regions — separately? The answers to these questions do not exist at present and will require the accumulation of a more complete data base.

5.5.3 Determination of Radiant Energies

5.5.3.1 Measured Energies of Different Components

For each of the prime flares, Table 5.5.1 gives the total radiant energies derived from the data in different energy or wavelength ranges. These observations do not cover the entire spectrum, as discussed in detail above. The table entries cannot be simply summed because of overlap, for example between the 0.5-4 Å and the 1-8 Å GOES broad-band soft X-ray entries. Suitable optical data were only available for a single flare (1980 November 5). By "suitable" we mean observations of Hα with sufficient spatial, temporal, and spectral coverage to permit a rough estimate of the excess radiation. Such data come either from the Multi-Slit Spectrograph (see Section 5.2) or else from Sacramento Peak CCD observations (e.g., Gunkler *et al.*, 1984), and unfortunately such observations are presently available only infrequently.

The purpose of Table 5.5.1 is to enable us to make intercomparisons among these observable components for these and other solar flares, and to allow us to make comparisons with other, possibly related, phenomena such as stellar flares.

5.5.3.2 Estimates of Total Radiant Energy

With these component radiant energies and the methods described above, we have made estimates of the broad components of total flare energy. These are given in Table 5.5.2, as measured by the three techniques: the direct estimations give the energy above 25 keV; the DEM analysis gives the soft X-ray energy, essentially 1 - 25 keV; and the scaling method gives the optical-EUV-XUV component. The typical uncertainties of these components are, respectively, 50%, 20%, and a factor of 10. For the direct estimates, the uncertainty comes from the photometric accuracy of the X-ray and gamma-ray detectors at higher energies; for the integrated energy above 25 keV this accuracy is dominated by the lack of spectral resolution in the determination of steep spectral distributions. In the soft X-ray region, we have a good check on the accuracy of the DEM approach from the broad-band soft X-ray photometry from GOES data. As noted in Section 5.3, the DEM in the 10^6 to 25 × 10^6K range tends to

Table 5.5.1 Component Radiant Energies (in ergs)

	Radiant Energy (ergs)				
Date in 1980 SXR Peak Time (UT)	**Apr 8 03:07**	**May 21 21:05**	**Jun 29 18:26**	**Aug 31 12:52**	**Nov 5 22:35**
> 1 MeV*	—	$<1\times10^{23}$	—	$<1\times10^{23}$	$<3\times10^{22}$
> 300 keV†	$<8\times10^{21}$	3×10^{22}	$<8\times10^{21}$	2×10^{22}	8×10^{22}
> 25 keV	1.5×10^{24}	1.1×10^{25}	1.1×10^{24}	1.2×10^{24}	2.8×10^{24}
0.5 - 4 Å	1.7×10^{28}	9×10^{28}	—	—	1.3×10^{28}
1 - 8 Å	1.9×10^{28}	6×10^{29}	1.0×10^{28}	—	8×10^{28}
Hα	—	—	—	—	2.3×10^{29}

*2σ upper limits based on nuclear gamma-ray line component, only.

†2σ upper limits and values from positive detections based on power-law fits to the observed continuum between 300 keV and 1 MeV, integrated to infinity.

Table 5.5.2 Total Energies (in ergs) of Component Radiations

Date 1980	SXR Peak Time (UT)	Soft X-ray T>2×10⁶K	Soft X-ray T>5×10⁶K	Soft X-ray T>10⁷K	Scaled T<2×10⁶K	Hard X-rays >25keV	Hα
8 Apr	03:07	—	—	1.1×10^{30}	—	1.5×10^{24}	—
21 May	21:05	—	5.8×10^{30}	2.6×10^{30}	—	1.1×10^{25}	—
29 Jun	18:04	—	—		—	5.4×10^{22}	—
	18:26	—	—	3.8×10^{30}	—	1.1×10^{24}	—
31 Aug	12:49	7.4×10^{28}	—	4.5×10^{27}	—	6×10^{23}	—
	12:52	7.6×10^{29}	—	5.6×10^{28}	—	6×10^{23}	—
5 Nov	22:28	—	1.3×10^{29}	5.1×10^{28}	—	3.3×10^{23}	
	22:35	—	4.0×10^{29}	2.9×10^{29}	1.8×10^{30}	2.5×10^{24}	2.3×10^{29}

show a bimodal distribution, with one "low-temperature" peak in the vicinity of normal active-region temperatures and one "high-temperature peak" above 10^7K. Since these are distinctly resolved, we have made separate entries for them. In the rest of the spectrum, there are insufficient data to estimate the uncertainties, and the result has little significance.

5.5.4 Comparison with Total-Irradiance Upper Limits

The radiant energies estimated in Table 5.5.2 could in principle be observed by using ACRIM. A preliminary search for flare effects in the ACRIM data was carried out by Hudson and Willson (1983), with the result that only upper limits could be established. Similar limits appear in Table 5.5.3 for the prime flares discussed above. These limits consist of comparisons between the SMM orbit containing the soft X-ray flare maximum and adjacent orbits; the data themselves appear in Figure 5.5.1. In no case was a significant excess detected. The table expresses the results in terms of 5σ upper limits on total radiant power and energy over the one-orbit interval indicated. Hudson and Willson (1983) give further details on the treatment of data.

Table 5.5.3 Comparison of ACRIM Upper Limits with Total Radiant Energy

Estimates for Prime Flares			
Date 1980	**Time interval (UT)**	**Power limit (10^{29} ergs s^{-1})**	**Energy limit (10^{32} ergs)**
Apr 8	02:29 - 03:24	3.2	5.0
May 21	20:48 - 21:47	2.7	4.4
Jun 29	18:04 - 19:03	2.1	3.4
Aug 31	12:34 - 13:31	1.8	3.0
Nov 11	22:06 - 23:03	2.1	3.4

5.5.5 Conclusions

The estimates of total radiant energy in the prime flares lie well below the ACRIM upper limits. This is consistent with our knowledge of the energy distribution in solar flares. Insufficient data exist for us to be very firm about this conclusion, however, and major energetic components could exist undetected, especially in the EUV-XUV and optical bands. In addition, the radiant energy cannot quantitatively be compared at this time with non-radiant terms because of even larger uncertainties in the latter.

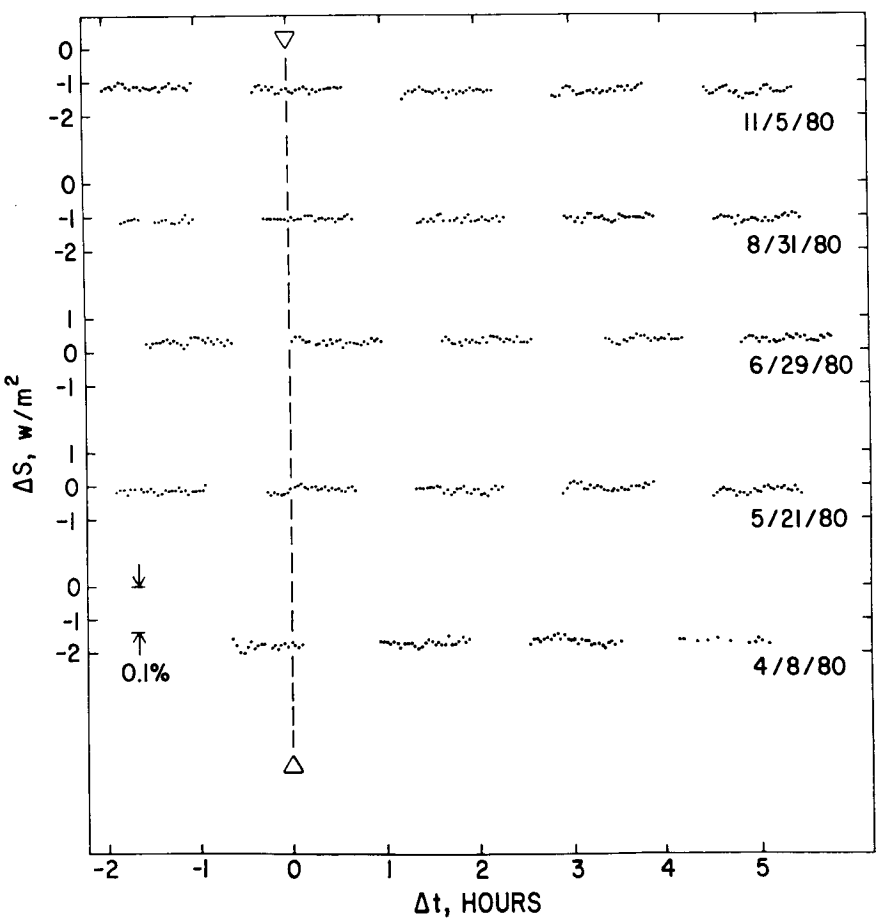

Figure 5.5.1 Radiant energy measured with ACRIM for 2 hours before and 6 hours after the prime flares listed in Table 5.5.3.

5.6 CONCLUSIONS

H.S. Hudson

5.6.1 Introduction

In this chapter we have tried to carry out a detailed accounting of the energy of a solar flare, intending that a clear view of the sources, sinks, and conditions for transport of energy would allow us to obtain a unique insight into the physics of flares. This tool was applied to several "key questions" stated in the introduction to this chapter, and in this section we give the responses to these questions as they appeared to follow from the energetics analysis. Unfortunately, the tool was generally not sharp enough — there are many key data missing from the observations — and the responses to the key questions are in some cases not definitive. As a result we have added a further section below, giving our suggestions for further observations needed to fill in the gaps and to give authoritative answers to the questions at some time in the future.

5.6.2 Responses to Key Questions

5.6.2.1 How Do We Characterize the Impulsive and Gradual Phases?

The classical definition of the impulsive phase depends on the presence of spiky (timescales of < 10 s) hard X-ray bursts (Kane 1969). The presence of this emission correlates well with the occurrence of microwave bursts whose spiky time profile, high polarization, and spectral maximum establish gyrosynchrotron radiation from energetic electrons as the emission mechanism. The microwaves thus serve as an effective substitute for the hard X-rays in defining the time of the impulsive burst.

The microwave spectrum also has an equivalent to the gradual phase, namely the "post-burst increase."The source of the post-burst increase is identified with the thermal soft X-ray source (Hudson and Ohki 1972). It is clear that this definitely "thermal" region — thermal in the sense of a Maxwellian, although optically thin, plasma — must coexist with the energetic electrons of the impulsive phase. A physically meaningful definition of the gradual phase therefore requires that the two phases overlap. We have therefore adopted this convention in describing flare energetics.

5.6.2.2 Do all Flares Have an Impulsive Phase?

The answer to this question is a qualified "yes," as judged from the correlation established between hard and soft X-ray occurrence shown in Figure 5.4.1 and 5.4.2. All of the flares considered fall near the correlation line with a scatter of ~ 0.5 (rms) in the logarithm. At the faint end, flares for which we have only upper limits on hard X-rays may appear to be purely thermal or gradual, but the absence of hard X-rays appears to be no more than a threshold effect within the bounds of the observed correlation.

One should note that a full answer to this question depends on knowing what defines a solar flare. Many flare-like effects appear in different environments, ranging from the photosphere to the middle corona, and extreme cases may exist that have not been selected as data for the correlation plot. It is quite clear that the Hinotori "B" and "C" flare classifications (see Section 5.1.5) represent distinctly different physical phenomena, for which there are different values for the hard/soft ratio.

5.6.2.3 What is the Total Energy Content of the Flare in the Impulsive Phase?

This question is discussed in detail in Section 5.2 and 5B.

5.6.2.4 What is the Relative Importance of the Thermal and Non-thermal Components of the Impulsive Phase of the Flare?

The thermal components of a flare often display a distribution of temperatures. In the later gradual phase, this distribution usually has relaxed into the bimodal emission-measure distribution described above, with peaks at about 3×10^6 and 15×10^6K. At earlier times, higher temperatures are best seen in data with high spectral resolution (Lin *et al.*, 1981). During the impulsive phase itself, the hard X-ray spectrum in the 20 to 100 keV range is often well represented by an isothermal, free-free emission spectrum. The same data may be equally well represented by a power law or by a broken power law. The distinction between thermal and non-thermal radiations therefore becomes quite fuzzy if based on the spectrum alone. The inclusion of the microwave data does not help very much, since the key low-frequency emission (i.e., the microwaves produced by the same electron population responsible for the hard X-rays) is optically thick to self-absorption and cannot yield physical parameters inside the source in a model-independent manner. On this basis, the present data alone are not sufficient to provide an unambiguous answer to this question.

One may go beyond the hard X-ray and microwave spectra to clarify the distinction between thermal and non-thermal distributions. Additional evidence from observations include time correlations with other emission such as EUV or white light, correlation with definitely non-thermal processes such as ion acceleration as represented by gamma-radiation; to this we may add insight gained from theoretical knowledge. This need to resort to secondary characteristics has historically resulted in enormous confusion and controversy, and it would be fair to state that at present this controversy continues unabated. The SMM observations and data obtained from other sources do not permit us to present a clear concensus answer to this question. The most likely scenario, however, is given in Section 5.5 of this chapter. The chief

result of this scenario is an answer to the key question under consideration, namely that non-thermal electrons accelerated during the impulsive phase have a dominant energetic role and that the thermal sources of soft X-rays are only one of several subordinate effects produced by this inherently non-thermal energy release.

5.6.2.5 How does the Gradual-Phase Energy Compare with the Impulsive-Phase Energy?

The answer to this question is model-dependent because of the ambiguity of the thermal/non-thermal question. We therefore give two answers in Table 5.6.1 based on the thermal [$E_{th}(>10^8K)$] and non-thermal [$W(>25keV)$] impulsive energies and the gradual thermal energies [$E_{th}(>10^7K)$] given in Table 5.2.7.

From Table 5.6.1 one can see that in the thermal case, the impulsive phase tends to be relatively unimportant and the main flare energy release occurs gradually throughout the duration of the flare. In the non-thermal case, it is possible that the impulsive phase contains a large fraction of the total flare energy.

Table 5.6.1 Ratio of Impulsive to Gradual Energies

Date 1980	Time (UT)	Thermal Ratio	Non-thermal Ratio
Apr 8	03:07	0.25	3.4
May 21	21:05	0.13	1.5
Jun 19	18:04	—	2.9
	18:26	1.6	1.1
Aug 31	12:49	3.0	1.5
	12:52	—	2.5
Nov 5	22:28	0.080.5	-4
	22.35	0.46	1.2

The "Thermal Ratio" is given by $E_{th}(>10^8K)/E_{th}(>10^7K)$ from Table 5.2.7.

The "Non-Thermal Ratio" is given by $W(>25keV)/E_{th}$ $(>10^7K)$ from Table 5.2.7.

5.6.2.6 What are the Dominant Cooling Mechanisms at Different Stages of the Gradual Phase?

The answer to this question depends crucially on the presence of unresolved fine structure in the soft X-ray sources. Decreasing the fluxtube diameter while holding the length and emission measure fixed requires higher densities, thus enhancing the radiative cooling rate. SMM has provided diagnostic evidence for small filling factors, but the observations are not comprehensive enough, nor at high enough spatial resolution, to permit this question to be answered in a model-independent fashion.

5.6.2.7 Do all the Post-Flare Loops Need Continual Energy Input?

In large, two-ribbon flares such as the 1980 May 21 flare, the reduction of the radiative cooling time due to filametary fine structure would worsen the discrepancy between the observed long cooling time and the predicted shorter time. Thus the SMM data confirm the need for continued energy input in the late phases of such flares, as reported in the Skylab workshop for the classical loop-prominence systems of the gradual phases of such flares. For compact flares, the observational situation is still vague.

The post-gradual phase phenomena found high in the corona after some major flares have an uncertain energetic link with the flare proper. At the other extreme, the "forerunner" of a coronal mass ejection sometimes appears to precede the associated flare. In both of these cases, there are simply insufficient data to understand the direction of energy transport or the forms of energy storage. These phenomena are energetically significant, however, and since they are remote from the flare it would be reasonable to assume that their energy sources are different.

5.6.2.8 Are There Extended, Late, Flare-Associated Sources in the Corona?

Yes, but there is no systematic knowledge of their relationship to the flares because of the lack of observations. They are energetically important.

5.6.3 Worthwhile Observations in the Future

The key questions addressed above are not sophisticated ones, and yet the present data have not proven capable of answering them all unambiguously. We can identify several reasons for this: first, the diagnostic capability of the available techniques is neither great enough nor fully executed in data of moderate resolution, such as those provided by the SMM observations. Second, the emphasis on diagnostic data has resulted in a lack of attention to basic data designed to define the energetics. Third, coronal observations have made insufficient technical progress and certainly have not provided an adequate data base. As a result, our knowledge of the physics of the lower corona above active regions is inadequate to define a correct conceptual model of flare evolution. Finally, the ground-based observatories have only begun to provide data that are sufficiently comprehensive to define morphology and energetics quantitatively. There is

much room for improvement in ground-based observations at optical wavelengths.

As is evident from the ambivalent answers to some of the key questions, the information presently available does not distinguish between thermal and/or non-thermal models of solar flares. To address that fundamental issue, observations are required with sufficient spatial and temporal resolution to distinguish between large thermal plasma volumes, on the one-hand, and beams of energetic electrons which stream through comparably large volumes at speeds of one third or more times the speed of light, on the other. These observations must be obtained in the appropriate spectral range to characterize mildly relativistic electrons, from several tens to several hundreds of keV.

Part of the resolution of these problems will come from the high resolution facilities planned for space in the future: the Solar Optical Telescope, the Pinhole/Occulter Facility, and other instruments leading up to the full-fledged Advanced Solar Observatory. However, it is a strong recommendation of this group that there be, in the next solar maximum, a renewed effort to obtain substantially improved ground-based observations at both optical and radio wavelengths.

5.6.4 Final Statement

This chapter has described our approach to understanding flare physics through analysis of the energy transport and storage in flares. Such an approach can only succeed if accurate, comprehensive data exist and can be understood in the context of a correct model for the flare phenomenon. Neither of these requirements has been met, and so the exercise has to be considered a failure. The introduction to this chapter describes the energy storage and flow in terms of the diagrams shown in Figure 5.1.1 and Figure 5.1.2. It would be safe to bet that not one single entry in these diagrams is presently known to better than an order of magnitude. Nevertheless, we feel that the attempt has been worth the effort, since by failing at this basic level to understand solar flares, we bring into question all more sophisticated channels of analysis.

Despite pessimism about our present state of knowledge, there is little doubt that remarkable progress has been made. We expect that a future exercise along these lines, hopefully during the forthcoming solar maximum, will be considerably more successful.

APPENDIX 5A. FLARES CHOSEN FOR THE ENERGETICS STUDY

G.M. Simnett, R.D. Bentley, P.L. Bornmann, M. Bruner, and B.R. Dennis

5A.0 Introduction

In this appendix we present brief descriptions of the flares which were chosen for the energetics study. A listing of the dates, times, locations, and classifications of these flares is given in Section 5.1 with the rationale for choosing this particular group of flares. More detailed discussions of these flares can be found in Sections 5.2 and 5.3.

5A.1 1980 April 8 at 03:04 UT

Bibliography: Antonucci, E. *et al.*, 1984, Ap.J., *287*, 917.
Cheng, C.C. *et al.*, 1982, Ap.J., *253*, 353.
Doschek G. *et al.*, 1981, Ap.J., *249*, 372.
Krall, K.R. *et al.*, 1983, Solar Phys., *79*, 59.
Machado, M.E. *et al.*, 1983, Solar Phys., *85*, 157.
Machado, M.E. and Somov, B.V., 1983, Adv. in Space Sci., *2*, 101.
Strong, K.T. *et al.*, 1984, Proc. of 25th COSPAR meeting, Graz, Austria.

This flare occurred in Hale region 16747 (Boulder no. 2372), which had been very active in the preceding days. The region was characterized by two large sunspots of opposite polarity, separated by a small, isolated bipolar area in a delta configuration. The longitudinal magnetic field is shown in Figure 5A.1, which also illustrates how the region changed during the preceding days. The isolated pole moved quite rapidly toward the leading sunspot in the days before April 8, leaving the magnetic neutral line highly deformed, with the transverse component of the field showing high magnetic shear.

The light curve for this flare is shown in Figure 5A.2, which illustrates the behavior of X-rays at 26-53 keV (HXRBS) and at 3.9 keV (BCS Ca XIX). Note that the hard X-ray flux observed before 03:03 UT is believed to originate from a different active region on the west limb, since no increase at that time was observed with the BCS or HXIS in their restricted fields of view. The relatively simple time profiles mask an extremely complex flare with a hierarchy of extended magnetic loop structures which became energized at different times and which had substantial temperature structure. Within the loops there appears to be a continuous evolution of the volumes confining the plasma, coupled with significant mass motions during the first few minutes of the impulsive phase. In fact, the maximum upflow of 310 km s^{-1} was observed around 03:04 UT, before the sharp increase in hard X-rays. The peak turbulent velocity was 120 km s^{-1}. One question we need to address is whether it is important to the flare energetics to consider the detailed morphology or whether it is adequate to analyze simply the full-flare light curves.

The spatial evolution of the flare as imaged in 11.5 to 16 keV X-rays is presented in Figure 5A.3 from the onset

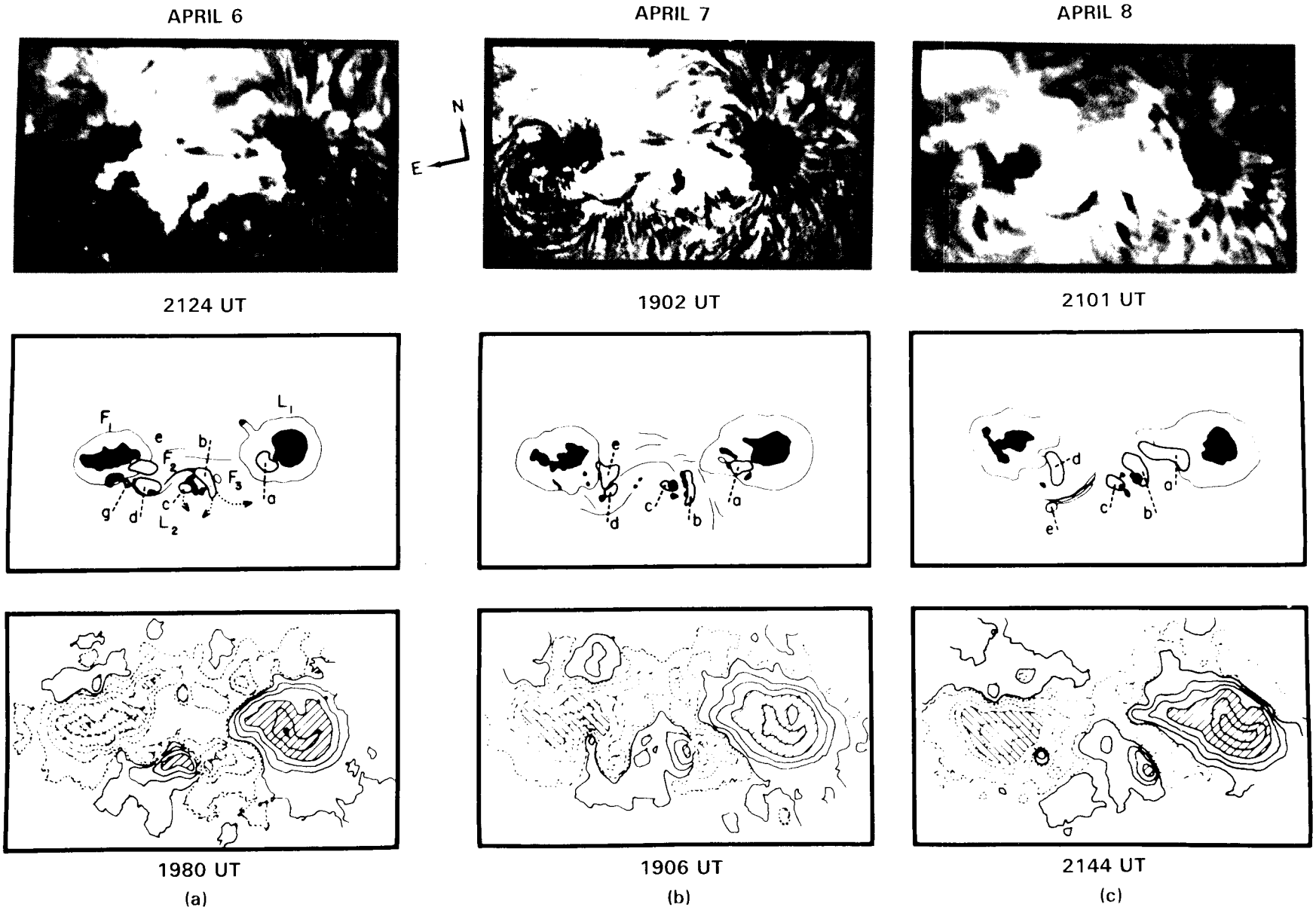

Figure 5A.1 This sequence of figures illustrates the development of Active Region 2372, including the period of the 1980 April 8 flare. The Hα filtergrams and sunspot drawings (courtesy M. McCabe) show the motion of the central bipole towards the leader spot. The equivalent MSFC magnetograms illustrate how the field changed and simplified as the region developed; the April 8 flare marked the end of this particular phase in the evolution of the region.

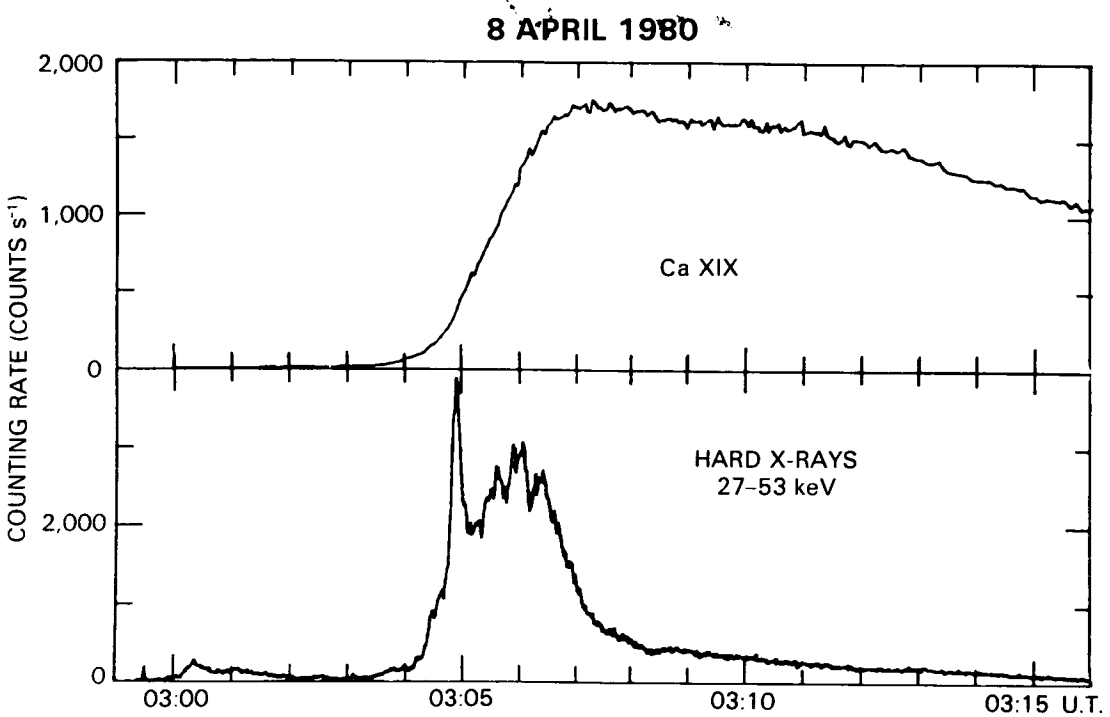

Figure 5A.2 Time profiles of the soft X-ray count rate in the BCS Ca XIX channel and the HXRBS channels 1 and 2 for the 1980 April 8 flare. Note that the hard X-ray flux peaking at 03:00:20 UT is not seen with BCS or HXIS and is believed to originate from a different active region on the west limb.

of the hard X-ray burst at 03:04:06 UT to late in the decay at 03:21:19 UT. The pre-flare brightening in fact starts as early as 02:45 UT and is followed by a second brightening from the same position at 02:59 UT, which leads into the impulsive phase. The position of the magnetic neutral line is drawn on Figure 5A.3(a); the pre-flare brightening is from the region of maximum shear in the transverse field. However, Figure 5A.3(c), which spans the peak in the hard X-ray burst, shows that the X-rays at that time came predominantly from two regions, with a secondary brightening to the east (left). This suggests a small, weak bipolar region that developed to the east of the neutral line near the large, trailing sunspot. The same two bright regions were resolved at 3.5-5.5 keV, before the peak in the hard X-ray burst. In the following minutes, the peak emission at all wavelengths shifted to an area between these two regions, and the hard X-ray emission entered a period of slow, monotonic decay. It was during this period that a region to the east brightened, and Figure 5A.3(h) shows the image accumulated between 03:12:20 and 03:13:57 UT, when this region had reached maximum intensity. There are three other resolved bright points in this image which are either persistent or visible at other wavelengths, or both.

5A.2 1980 May 21 at 20:53 UT

Bibliography: Antonucci, E. and Dennis, B.R. 1983, Solar Phys, *86*, 67.
Antonucci, E., Dennis, B.R., Gabriel, A.H., and Simnett, G.M., 1985, Solar Phys., in press.
Antonucci, E., Gabriel, A.H., and Dennis, B.R., 1984, Ap.J., *287*, 917.
Bely-Dubau *et al.*, 1983, MNRAS, *201*, 1135
Duijveman *et al.*, 1982, Solar Phys., *81*, 137.
Duijveman, A. 1983, Solar Phys., *84*, 189.
Harvey, J.W., 1983, Adv. in Space Res., *2*, 31.
Hoyng, P. *et al.*, 1981, Ap.J., *246*, L155
Svestka, Z. *et al.*, 1982, Solar Phys., *75*, 305.
Svestka, Z. *et al.*, 1982, Solar Phys., *78*, 271.

This event was a classical two-ribbon flare, starting with filament activity above the magnetic neutral line that led into the impulsive phase as the filament started to rise. It was

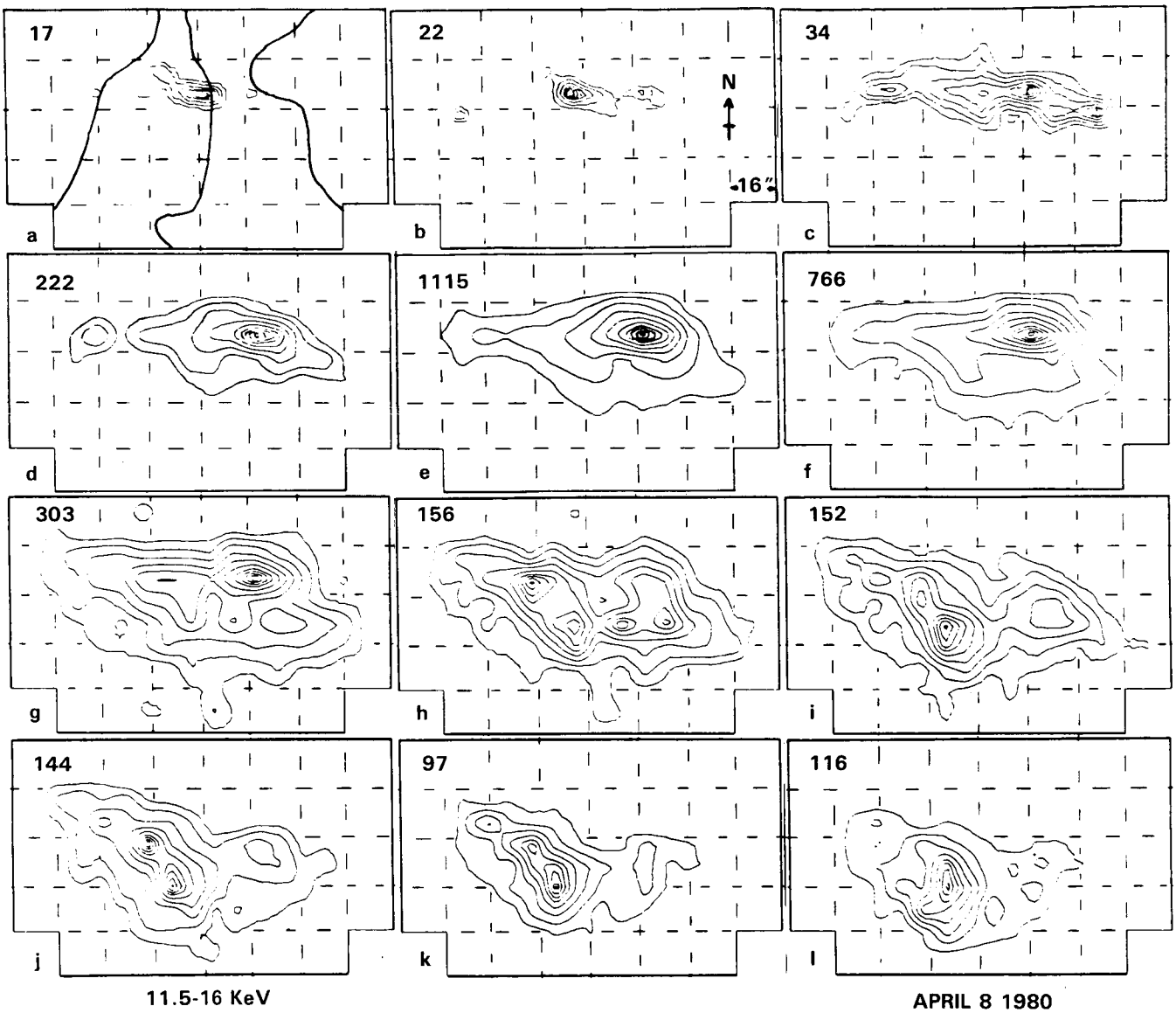

Figure 5A.3 Contour maps of the 11.5 to 16 keV X-ray flux for the 1980 April 8 flare at the following times: (a) 03:04:06 – 03:04:22, (b) 03:04:24 – 03:04:44, (c) 03:04:46 – 03:05:05, (d) 03:05:07 – 03:06:16, (e) 03:06:21 – 03:08:34, (f) 03:08:39 – 03:10:25, (g) 03:10:30 – 03:12:15, (h) 03:12:20 – 03:13:57, (i) 03:14:03 – 03:15:47, (j) 03:15:52 – 03:17:39, (k) 03:17:43 – 03:19:29, (l) 03:19:34 – 03:21:19 UT. These maps were obtained from the HXIS data by deconvolving the collimator response using the iterative technique described by Svestka *et al.* (1983).

from Hale region 16850, which had produced only subflares with very weak X-ray emission during the previous 100 h; similarly, it was followed by small, weak flares. This was therefore an example of an isolated large flare. The intensity time profile is shown in Figure 5A.4 for 27 to 54 keV X-rays (HXRBS) and the Ca XIX channel (BCS). Once the thermal phase of the flare began, the plasma had an extremely hot component, exceeding 30×10^6K, until late in the decay phase.

Figures 5A.5(a) and (c) show the appearance of the flare region in Hα both before and during the main phase of the flare, and Figures 5A.5(b) and (d) show magnetograms for two times before the flare. The bulk of the 16 to 30 keV X-rays during the main impulsive hard X-ray spike appear at position A, with a significant second bright point at B about 27000 km away on the other side of the filament. The 16 to 30 keV X-ray features are superimposed on Figure 5A.5(a) to illustrate this. The X-ray images have been interpreted

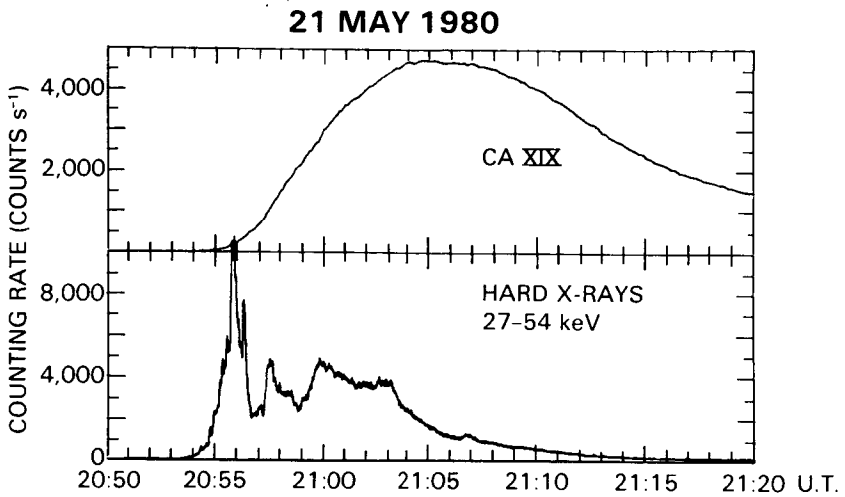

Figure 5A.4 Same as Figure 5A.2 for the 1980 May 21 flare.

as providing the first observational evidence of footpoint brightening from the chromospheric base of a magnetic loop caused by deposition of non-thermal particles (Hoyng *et al.*, 1981).

In addition to the hard X-ray features, HXIS studied the morphology of the soft X-ray emission above 3.5 keV, both along and across the filament, as the flare evolved. By 20:48 UT, the soft X-ray flux was enhanced along the filament, which had begun to separate at that time. In this pre-flare period there was already soft X-ray emission from A (Figure 5A.5), which appeared as a barely resolved magnetic loop at the site of the newly emerged magnetic flux. There were many resolved X-ray bright points early in the flare, suggesting a variety of magnetic loops. These disappeared at the onset of the impulsive phase just after the filament began to rise.

The Ca XIX line profile began to exhibit the signature of mass motion during this period, and a series of line scans is presented in Figure 5A.6. At 20:53 UT the entire soft X-ray source is observed to be moving upwards at 80 km s^{-1}. By 20:57 UT the motion of the bulk plasma flow diminished to the lowest detectable value of 30 km s^{-1}. However, at the start of the first hard X-ray burst, additional material was injected at a velocity of 370 km s^{-1}, and this is observed as a separate feature in the blue wing of the resonance line in Figure 5A.6(b). This high velocity upflow coincided with a spectral hardening of the X-ray emission to the power law index of -4, a value maintained until 21:04 UT. The detection of blue-shifted material continues to 21:05 UT. Therefore, the energy driving the upflow appears to be deposited in the chromosphere for as long as the spectral index remained around -4, but no longer.

A type II radio burst starts at 20:57 UT, and the flare generated a prompt, energetic (>40 MeV) proton event at 1 AU plus a traveling interplanetary shock which accelerated low energy protons as it moved outward. A type I radio noise storm was seen during the early hours of this motion, accompanied by weak soft X-ray emission from a large (> 105 km radius) coronal arch located above the flare site. The arch was visible in soft X-rays for over 10 h.

5A.3 1980 June 29 at 18:03 and 18:22 UT

Bibliography: Bentley, R.D. *et al.*, 1984, Solar Phys., in preparation.
Harrison, R.A. *et al.*, 1985, Solar Phys., submitted.
Poland, A.I. *et al.*, 1982, Solar Phys., *78*, 201.
Schmahl, E.J., 1983, Adv. in Space Sci., *2*, 73.
Simnett, G.M. and Harrison, R.A., 1984, Proc. 25th COSPAR meeting, Graz, Austria.
Simnett, G.M. and Harrison, R.A., 1984, Solar Phys., (submitted).
Wu, S.T. *et al.*, 1983, Solar Phys., *85*, 351.

These two flares are discussed together, since they are related by the coronal disturbances seen both in white light and at X-ray and radio wavelengths. After the first flare at 18:03 UT, a coronal X-ray source was observed by HXIS to move slowly outwards. A coronal mass ejection was detected by C/P until 20:03 UT, and the onset of the event was observed with the Mark-3 K-Coronometer on Mauna Loa from around 18:18 UT, several minutes before the onset of the second (main) flare at 18:22 UT. However, a type II radio burst was only observed for a few minutes from 18:33 to 18:36 UT, and from the observed drift rates it appeared to be associated primarily with the second flare. The velocity measured by the K-Coronameter is 500 km s^{-1} and the velocity derived from the type II burst is 1100 km s^{-1}. The observations are summarized in Figure 5A.7, which shows

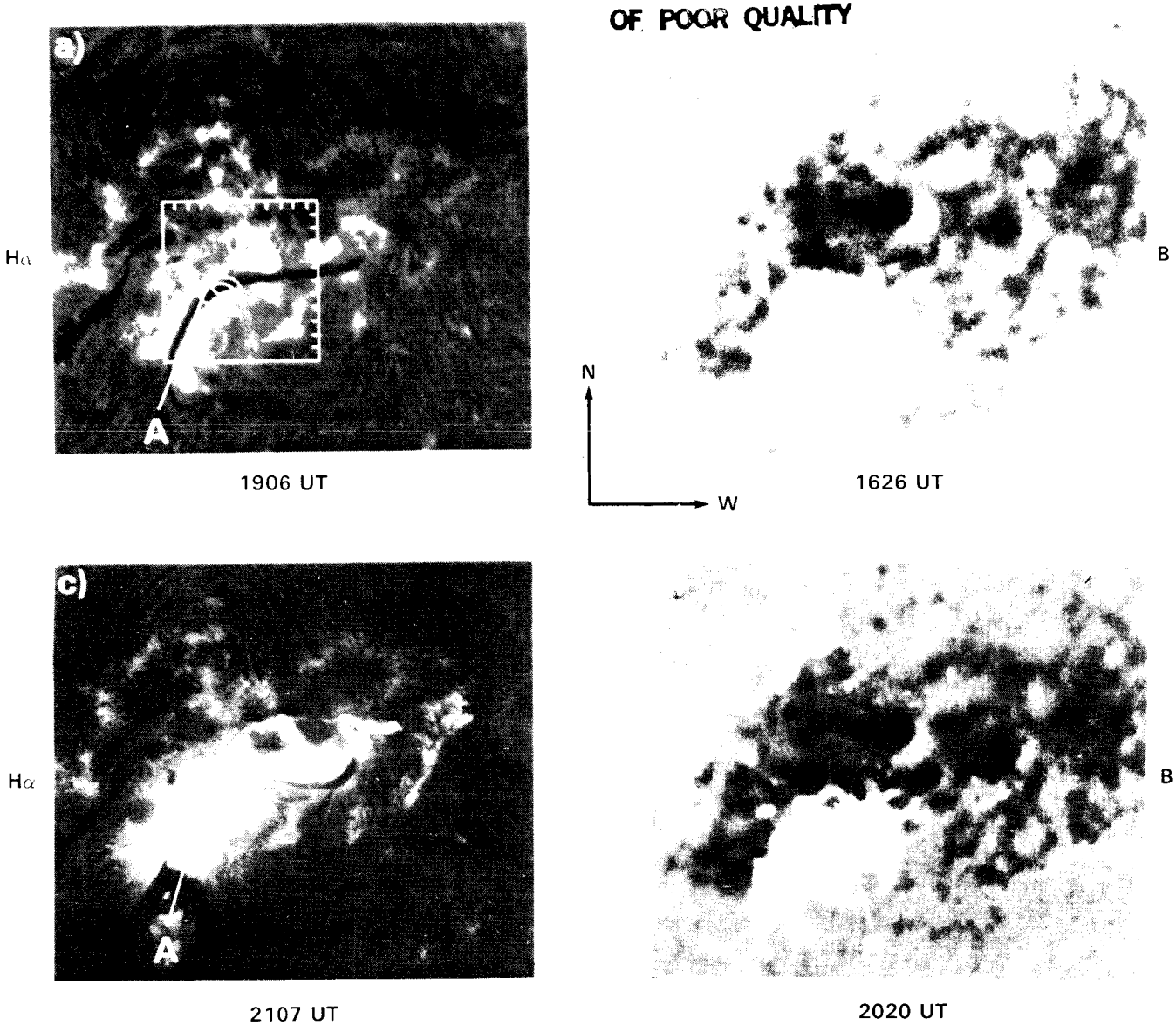

Figure 5A.5 Hα images and magnetograms for the 1980 May 21 flare from Hoyng *et al.* (1981). (a) The Hα image at 19:06 UT with the contours of the 16 to 30 keV X-ray bright patches superimposed. The X-ray bright patches were observed with HXIS during the two main hard X-ray peaks at 20:56 UT. The frame around the X-ray contours measures 96 × 96 arcsec. (b) Line-of-sight component of the underlying magnetic field at 16:26 UT. (c) The Hα flare at 21:07 UT. (d) The magnetic fields at 20:20 UT. 'A' marks the location of the new sunspot (positive flux), and B gives the location of new negative flux.

the intensity-time profiles for 28 to 55 keV X-rays (HXRBS) and the Ca XIX channel (BCS).

Although both flares occurred on the west limb, they were not from precisely the same location. The first flare was centered approximately 16 arc sec south of the main flare and occurred in coincidence with a subflare from S11 W36, which reached a maximum in Hα at 18:06 UT. The first flare was still visible in soft X-rays when the second flare started. For many hours previously, a large system of loops stretching high into the corona was visible with both HXIS and FCS.

Figure 5A.8 shows the development of the flares as observed in various wavelengths ranging from Hα to Mg XI. Figure 5A.8(a) is an FCS image in Mg XI taken from 18:08:08 to 18:13:07 UT; the dotted line marks the position of the limb as seen by the FCS white-light sensor. The actual limb would be the best-fit smooth curve through these points. The position of the UVSP field of view is outlined in the NW corner. Figure 5A.8(b) shows a smaller FCS raster, again in Mg XI taken from 18:26:27 to 18:30:54 UT, covering the initial decay of the second flare. The enhanced coronal

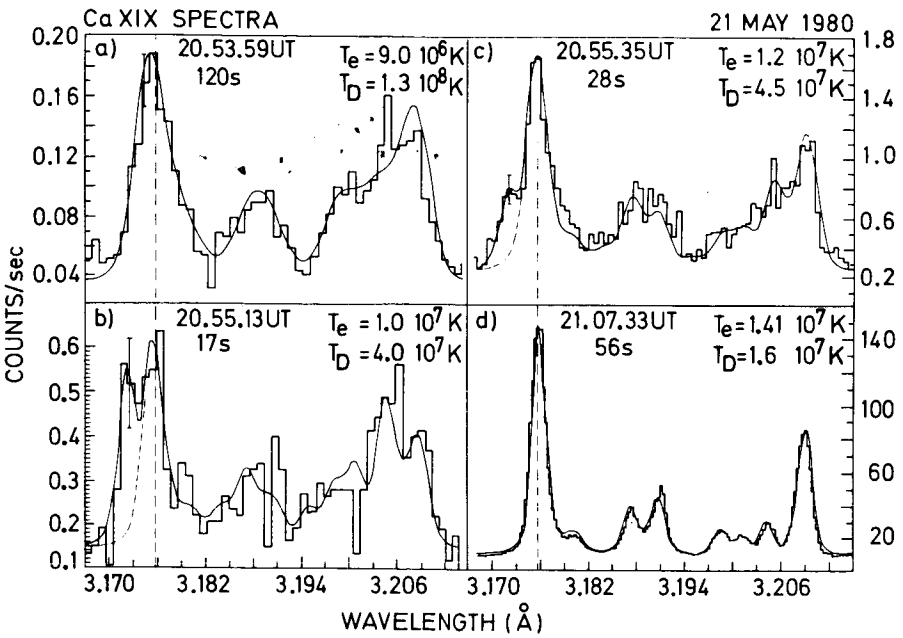

Figure 5A.6 Sequence of soft X-ray spectra obtained at four times during the impulsive phase of the 1980 May 21 flare in the BCS channel covering the Ca XIX spectral region from 3.165 to 3.231 Å. The smooth curve in each figure represents the synthesized spectrum computed for given values of the electron temperature T_e and the Doppler temperature T_D. In (b) and (c), two synthesized spectra, with one blue-shifted by 3.8 mÅ, are summed to form the spectrum represented by the smooth curves. The dashed lines in the same figures represent the profile of the principal component expected for the given Doppler temperature. The time given for each spectrum is the mean time of the observation interval, and the accumulation period is given below this time.

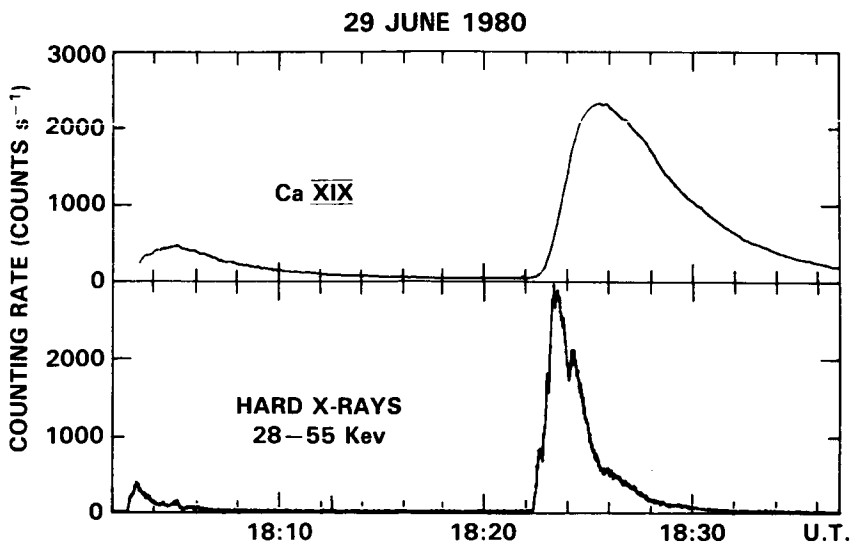

Figure 5A.7 Soft (top) and hard (bottom) X-ray time profiles for the 1980 June 29 flares similar to Figure 5A.2. Note that SMM emerged from night at 18:02:40 UT during the first of the two flares.

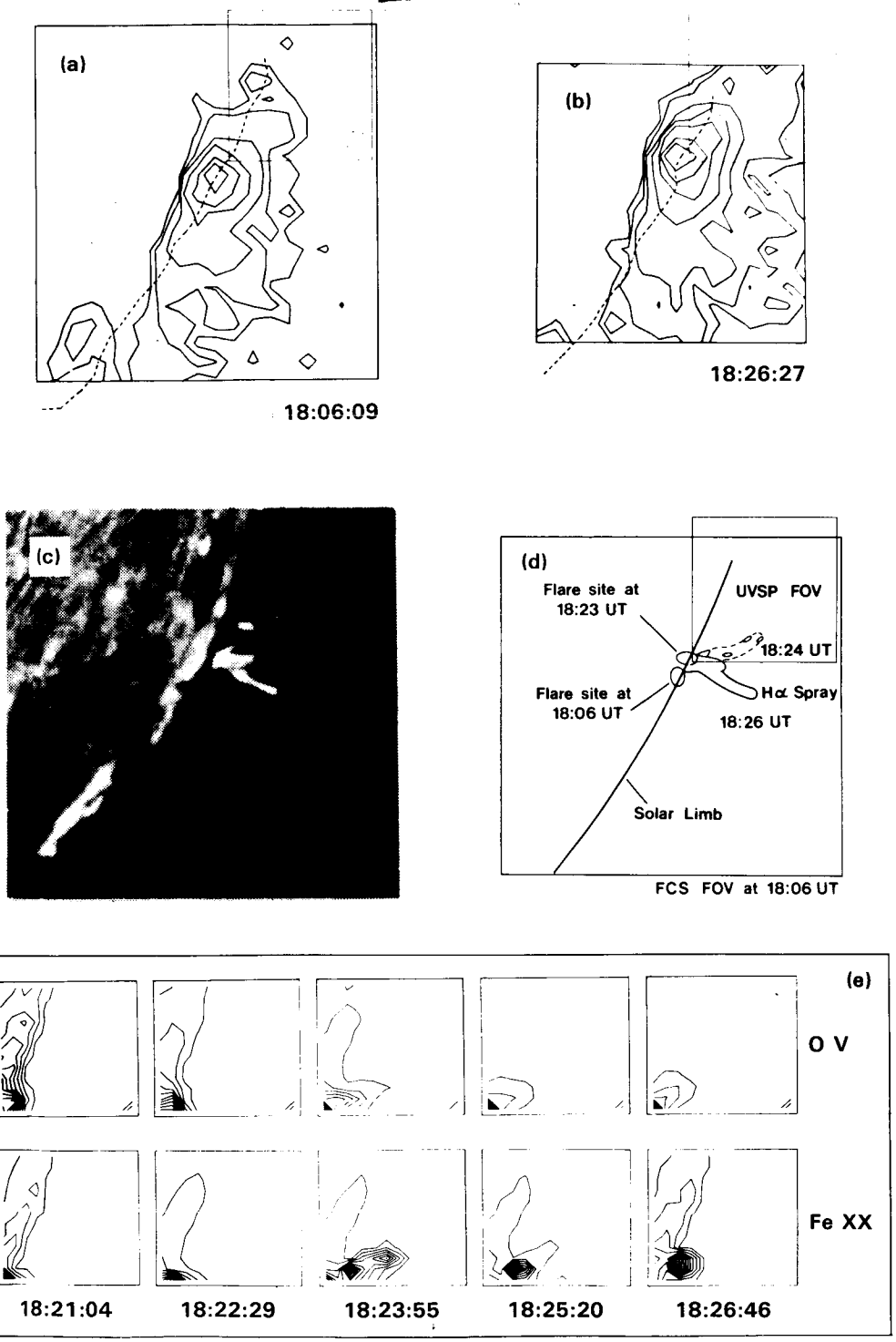

Figure 5A.8 Images of the 1980 June 29 flares in different wavelength ranges at the UT times indicated. (a) FCS image in Mg XI during the first flare. The dotted line marks the position of the limb as seen by the FCS white light sensor. The UVSP field of view is shown in the NW corner of the image. (b) Similar to (a) for the second flare. (c) Hα picture taken at the Ramey Observatory at 18:20 UT during the second flare. (d) Sketch of the solar limb and lower corona summarizing the imaging observations of the two flares. (e) UVSP images in OV and Fe XXI during the second flare.

X-ray emission is clearly visible in both images. Figure 5A.8(c) shows an Hα picture taken at the Ramey Observatory at 18:26 UT. This follows a small bright limb surge at 18:20 UT, after which a mass of ejected material, subtending 3 arc min at the Earth, became visible. The origin of the second flare is just beyond the west limb. Figure 5A.8(d) is a sketch of the solar limb and lower corona, summarizing these observations.

Figure 5A.8(e) shows UVSP images in O V and Fe XXI during the rise and decay of the second flare. There is clearly a path into the corona to the northwest during the initial stage of the flare, which became less prominent following flare maximum. This is consistent with the southerly swing seen in Hα.

The hard X-ray burst shown in Figure 5A.7 consists of a series of spikes, followed by a smooth, slow decay from 18:25:30 UT. The X-ray spectrum is hardest during the initial rise. The microwave emission shows similar multiple spike structure, and the burst was strongly right-circularly polarized with a peak frequency of 2.2 GHz. At the onset of the second flare, a series of type III and V radio bursts was observed in coincidence with a blue-shifted feature seen in the Fe XXV line profile. This is coincident with the southerly swing in the Hα spray, suggesting that the motion of the spray had a significant longitudinal component in the solar reference frame.

5A.4 1980 August 31 at 12:48 and 12:52 UT

Bibliography: Strong, K.T. *et al.*, 1984, Solar Phys., *91*, 325.

These flares involved two distinctive and separate energy releases in a compact flare region which produced quite different responses in the radiated emissions and mechanical mass motions. The longitudinal magnetic field structure of the region is shown in Figure 5A.9(a), in which a negative intrusion is visible between the two leading positive sunspots. Figure 5A.9(b) shows the magnetic neutral line and the positions of maximum shear in the longitudinal field. It is from one of these highly sheared regions that the bright flare points A, B, and C occurred, whereas a weak brightening at D shows that there was some interaction with more distant parts of the region.

Figure 5A.10 presents the time profiles for 28 to 500 keV X-rays, the Ca XIX resonance line (3.176 Å), and the microwave intensity at 15.4 GHz. The gross differences between these curves have proved valuable in interpreting the vari-

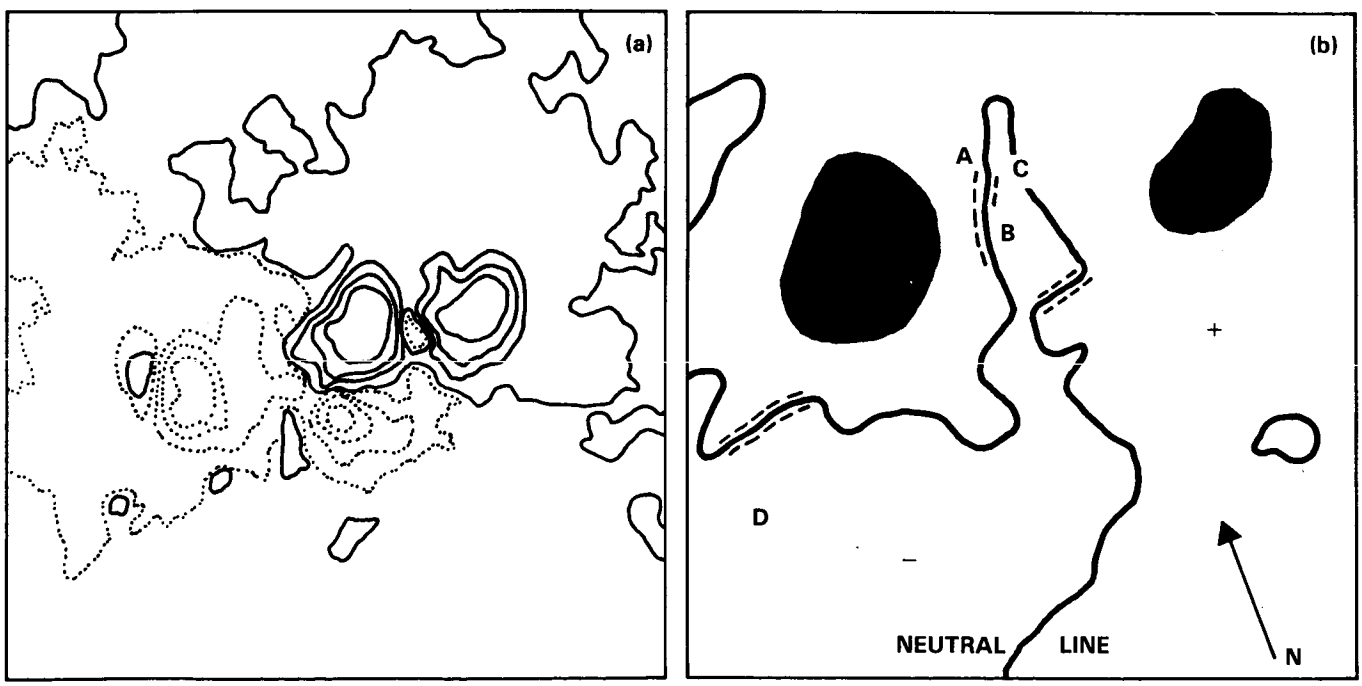

Figure 5A.9 The magnetic structure of NOAA Active Region 2646. (a) A magnetogram showing the longitudinal fields; note the location of the three sunspots, and the small negative intrusion between the two leading positive spots. Positive and negative polarities are indicated by solid and broken lines, respectively. The magnetogram is approximately 4 arc min square. (b) A schematic diagram of the flare site showing the location of the spot umbrae (shaded area), the neutral line (solid line), and the areas of maximum shear in the transverse field component (dashed lines). The main sites that are discussed in the text are labeled A-D.

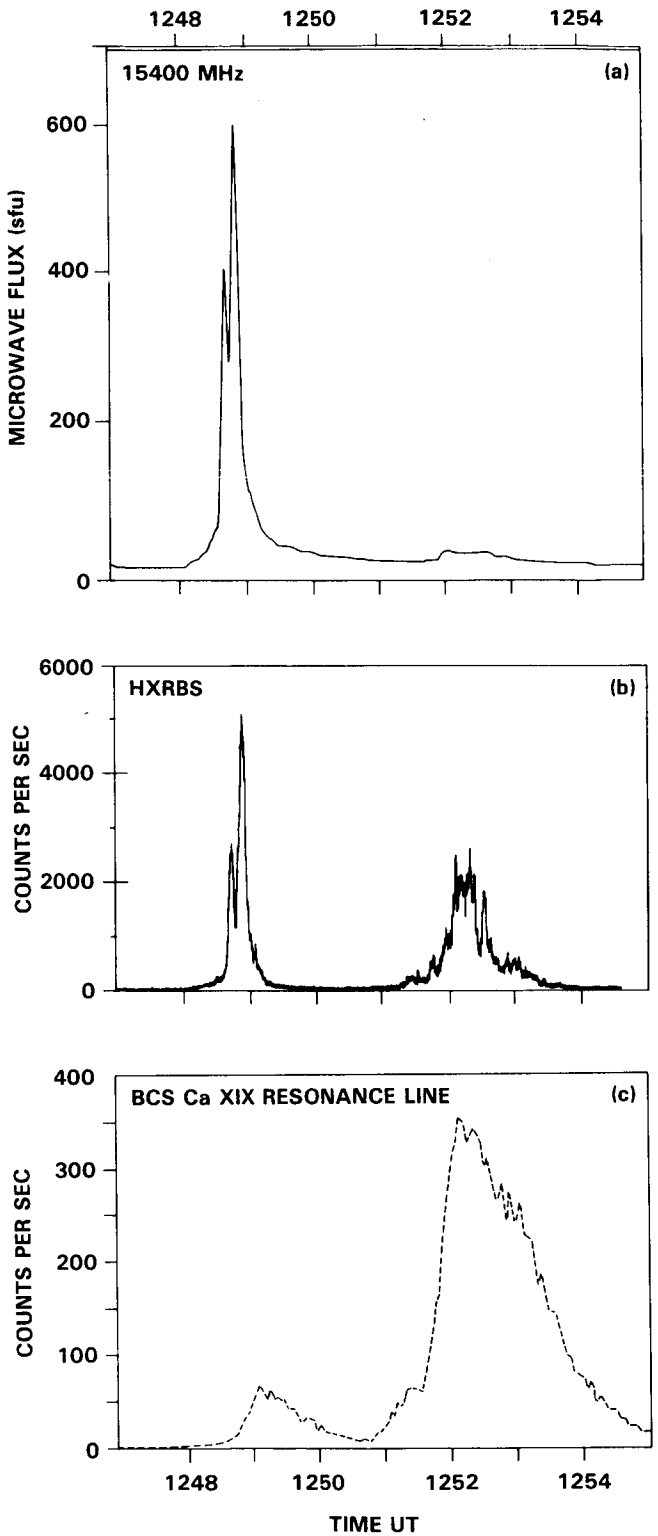

Figure 5A.10 Light curves of the two flares on 1980 August 31. (a) Microwave flux at 15.4 GHz. (b) Hard X-ray (>28 keV) count rate. (c) Soft X-ray (Ca XIX resonance line at 3.176 Å) light curve. Note the variation in the relative brightness of the two flares at various wavelengths.

ous modes of energy release and energy transport. In the first flare, the impulsive emissions show two main spikes, one at 12:48:42 UT and the other at 12:48:51 UT. The Ca XIX emission was delayed significantly; the peak intensity occurred at 12:49:06 UT, by which time the impulsive emissions had decayed by an order of magnitude from their peak.

In contrast, the onset of the second flare was more noticeable in Ca XIX than in hard X-rays or microwaves, and there was a precursor rise, which by 12:51:25 UT had reached a level equal to the maximum of the first flare (see Figure 5A.10). It was accompanied by a weak increase in hard X-rays but no discernable change in the microwave flux. At 12:51:35 UT the main Ca XIX increase started, this time accompanied by hard X-ray emission but a relatively weak microwave event. The unusual features of the second flare were the close temporal correspondence of the peaks of the Ca XIX and hard X-ray emission and the rapid decay of the Ca XIX emission. There was also a large variation in the brightness of the second flare compared with that of the first at different wave-lengths. In hard X-rays (>28 keV) and in 15.4 GHz microwaves, the second flare was weaker by a factor of 2 and 33 ± 6, respectively. In soft X-rays, the second flare was brighter by a factor of 5.8 in the Ca XIX resonance line, 3 in O VIII, and 8 in Fe XXV. The flares occurred at slightly different locations within the active region, as can be seen from the X-ray images in Figure 5A.11. The first flare, shown in an 8 to 16 keV image in Figure 5A.11(a), had two bright points aligned approximately E-W and on either side of the neutral line. The 16 to 30 keV image confirmed this. There was a blue shift in Ca XIX corresponding to a velocity of 60 ± 20 km s^{-1} and a line broadening corresponding to a turbulent velocity of 190 ± 40 km s^{-1}. A blue shift, corresponding to a velocity of around 180 km s^{-1} was also seen with UVSP in the Fe XXI line at 1354 Å, whereas the line broadenings were equivalent to turbulent velocities in the range 66-150 km s^{-1}.

The hard X-rays at the onset of the second flare shown in Figure 5A.11(b) were from an area to the north near point A of Figure 5A.9(b). They subsequently appeared at a point about 6 arcsec to the south [Figure 5A.11(c)] very close to the eastern bright point shown in Figure 5A.11(a). There were no indications of significant blue shifts from the second flare. In fact, to the contrary, the blend of O I and C I at 1355.8 Å observed with UVSP had the red wing enhanced, suggesting downflows of material at chromospheric temperatures. On account of the different locations and the very distinct characteristics of the two flares, it seems that heated plasma from the first flare broke out of the flare loop into an adjacent structure to the north, where it triggered the release of a larger amount of energy to produce the second flare. However, the evolution of the first flare resulted in a completely different set of starting parameters, such as densities and temperatures, governing the development of the second flare.

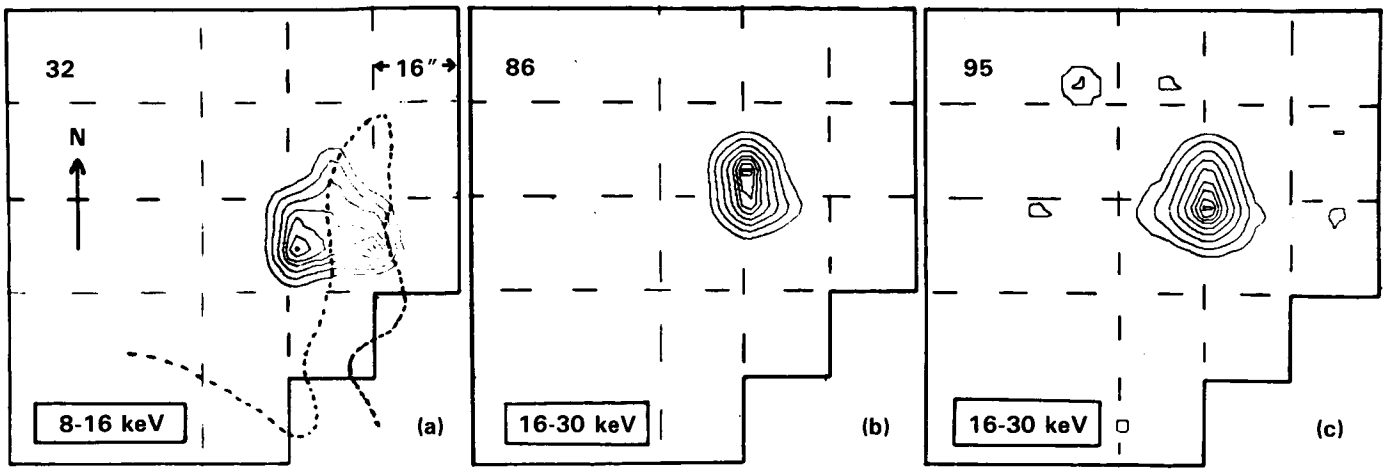

Figure 5A.11 HXIS contour plots showing the location of the hard X-rays at the times indicated during the two flares on 1980 August 31. The contours were obtained by deconvolving the collimator response with the iterative technique described by Svestka *et al.* (1983). The dotted line in (a) shows the location of the magnetic neutral line.

The X-ray spectrum is very similar in shape at the hard X-ray peaks in both flares. The principal difference lies in the region below 15 keV, which is considerably enhanced at the peak of the second flare. In this region the emission is dominated by thermal radiation at $(20 \pm 5) \times 10^6$ K.

5A.5 1980 November 5 at 22:26 and 22:33 UT

Bibliography: Bornmann, P.L., 1985a, Ap.J., in press.
Bornmann, P.L., 1985b, Solar Phys., submitted.
Dennis, B.R. *et al.*, 1984, Proc. 2nd Indo-US Workshop on Solar Terrestrial Physics, New Delhi, India.
Duijveman, A. *et al.*, 1982, Solar Phys. *81*, 137.
Duivjeman, A. *et al.*, 1983, Solar Phys. *88*, 257.
Hoyng, P. *et al.*, 1983, Ap.J. *268*, 865.
Martens, P.C.H. *et al.*, 1985, Solar Phys., *96*, 253.
Phillips, K.J.H. *et al.*, 1982, Ap.J. *256*, 774.
Rust, D.M. *et al.*, 1985, Ap.J., *288*, 401.
Rust, D.M. and Somov, 1984, Solar Phys., *93*, 95.
Wolfson, C.J. *et al.*, 1982, Ap.J. *269*, 319.

These two flares occurred in Hale region 17244 (Boulder no. 2776), which included a group of sunspots in a delta configuration (opposite polarity umbra within a single penumbra). For at least 20 min before the onset of the first flare, there was 3.5 to 5.5 keV X-ray emission from the photospheric magnetic neutral line, with occasional bright points at places which subsequently featured prominently in the main flare. The intensity-time profiles are shown in Figure 5A.12 for 29 to 57 keV X-rays (HXRBS) and 3.5 to 5.5 keV X-rays (HXIS).

These two flares are included in our study because of the complete data coverage available. Ground-based optical, magnetogram, and radio data augment the satellite data from SMM and GOES. The entire flaring region was observed with HXIS, HXRBS, and ground-based stations. Although BCS was turned off during the decay of the second flare, data were available at all other times. This flare was also chosen because density diagnostics are available from the FCS data. The FCS was pointed at the brightest point in the flare, covering a 14 × 14 arcsec (FWHM) portion of the entire flaring region. The UVSP observed another portion of the flare, which did not overlap with the region seen by FCS. The VLA observed all of the first flare but only the decay of the second flare.

The flares were well observed with the Hα Mulitslit Spectrograph at Big Bear Solar Observatory and consequently are illustrated by these observations in somewhat greater detail than is available for the other flares. Figures 5A.13(a) and (b) show a sequence of images of the two flares in both centerline Hα and HeI D_3 at 5876 Å. Both flares were classified as two-ribbon flares, although the ribbons remained

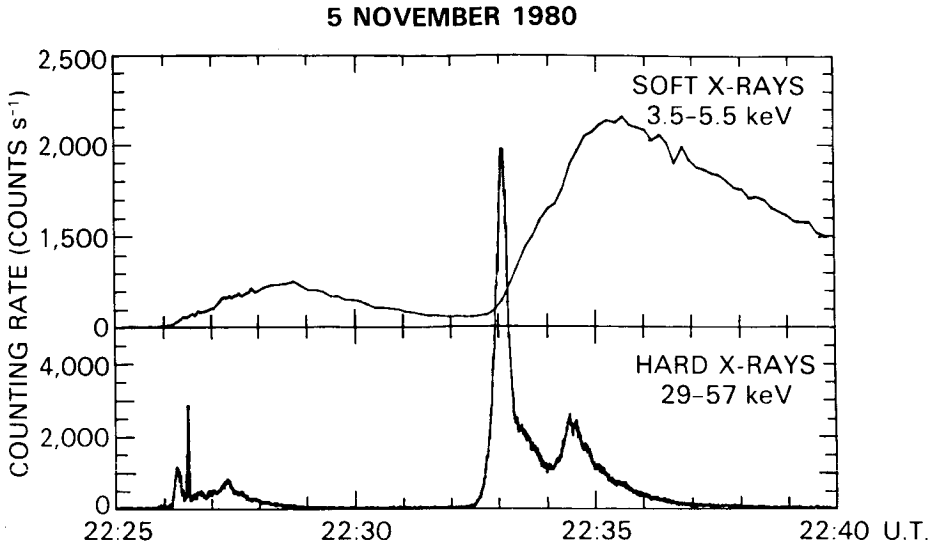

Figure 5A.12 Time profiles of the soft X-ray counting rate in HXIS band 1 (3.5 – 5.5 keV) and in HXRBS channels 1 and 2 (29 – 57 keV) for the two flares on 1980 November 5. The HXIS counts were from selected coarse-field pixels and the rate was corrected for the instrumental dead time.

stationary and did not separate during either flare. The flares were nearly cospatial and can be regarded as homologous; the main difference between them lies in their overall brightness.

Several important features are apparent from the Hα and HeI D_3 observations:

- The HeI D_3 emission points began at the same time as the >28 keV X-rays and continued for approximately the same duration in both flares (see Figure 5A.14).
- The temporal fine structure seen in hard X-rays is also a property of the HeI D_3 emission; each emission point was relatively short lived, usually lasting no more than 1 min.
- Both flares were a succession of many rapidly forming and decaying bright points extending on both sides of the flare kernels. The last of the bright points to develop were those most distant from the kernels, and they were the least bright. The exception was the bright point to the northeast, which peaked in intensity around 22:33:09 UT, slightly later than the hard X-ray peak from this location as discussed below.
- The flare sites which had bright HeI D_3 emission also had Hα line profiles typically more than 3Å wide (FWHM).
- After the initial brightening of the Hα kernels in the second flare, a rebrightening occurred coincident with the secondary hard X-ray maximum at about 22:34:20 UT (Figure 5A.12).

The first flare at 22:26 UT has been studied by Hoyng *et al.* (1983) with optical, hard X-ray (HXIS), and microwave (VLA) images. Figures 5A.15 (a) and (b) are sketches of the center of the active region showing the locations of the various flare components in Hα and HeI D_3 relative to the neutral line. The 15-GHz source and the boundaries of the prominent HXIS pixels are also indicated. The region appears to consist of a set of low-lying loops, probably highly sheared, whose footpoints lie in the Hα strands S1 and S2. Above these loops is an overlying loop whose footpoints appear to be in the Hα kernels labeled a and e in Figure 5A.15(b). The VLA images show a bright area that lies across the neutral line at the center of the flaring region. This 15-GHz source had a circular polarization of up to 80% during the first flare with a brightness temperature of $>10^9$K. The sense of polarization reversed at the magnetic neutral line. The evolution of the hard X-ray images during the first flare is shown in Figures 5A.16(a), (b), and (c). At the onset of the first flare [Figure 5A.16(a)], the majority of the 16 to 30 keV photons came from the position labeled B in Figure 5A.16(b), which is coincident with the location of the bright He ID_3 kernels. By the time of the narrow intense spike at 22:26:30 UT (Figure 5A.12), the hard X-rays were coming from the position labeled T in Figure 5A.16(b), coincident with the location of the microwave source. The 22 to 30 keV image from 22:26:12 to 22:26:38 UT [Figure 5A.16(b)] shows emission from points A, B, and T. It is presumed that T is at the top of the magnetic loop with footpoints at A and B. This loop was situated over the smaller loops which presumably linked the bright Hα strands S1 and S2. Hoyng *et al.* (1983) estimated that the magnetic field at the neutral line was 700 ± 160 and 480 ± 110 G during the first two hard X-ray peaks, respectively. The loop AB is in-

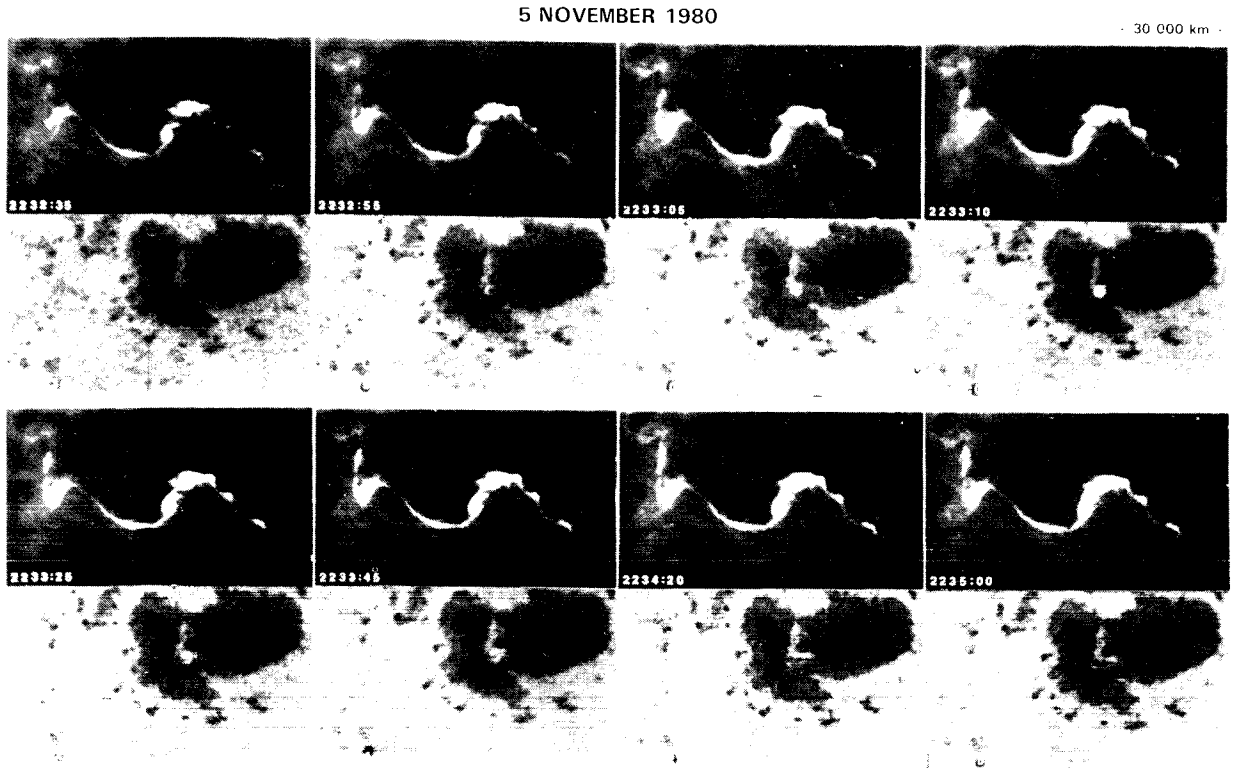

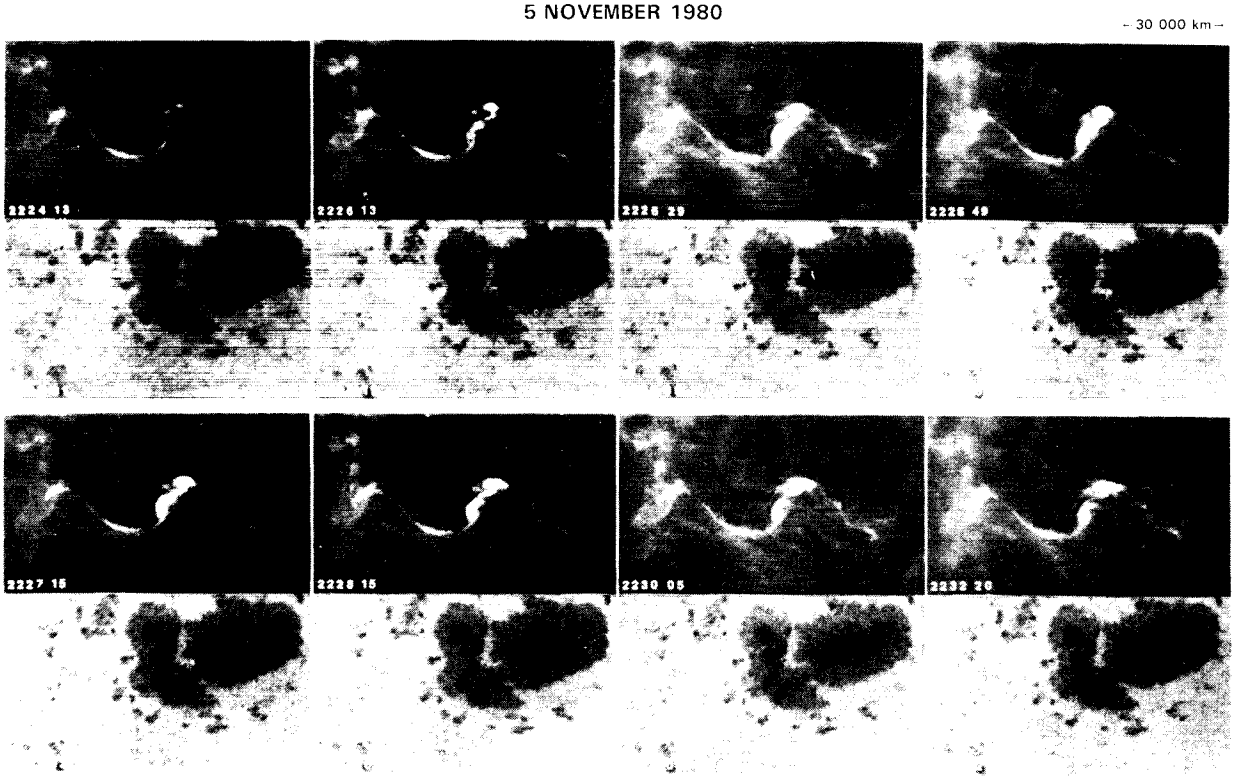

Figure 5A.13 (a) Images of first of the two 1980 November 5 flares in Hα and in HeI D_3 taken at the times indicated. The first and third rows of photographs are Hα center-line images, and the second and fourth rows are HeI D_3 images. (b) As for Figure 5A.13(a) for the second flare on 1980 November 5. Note that this flare began during the decay of the earlier flare and followed the same pattern of development.

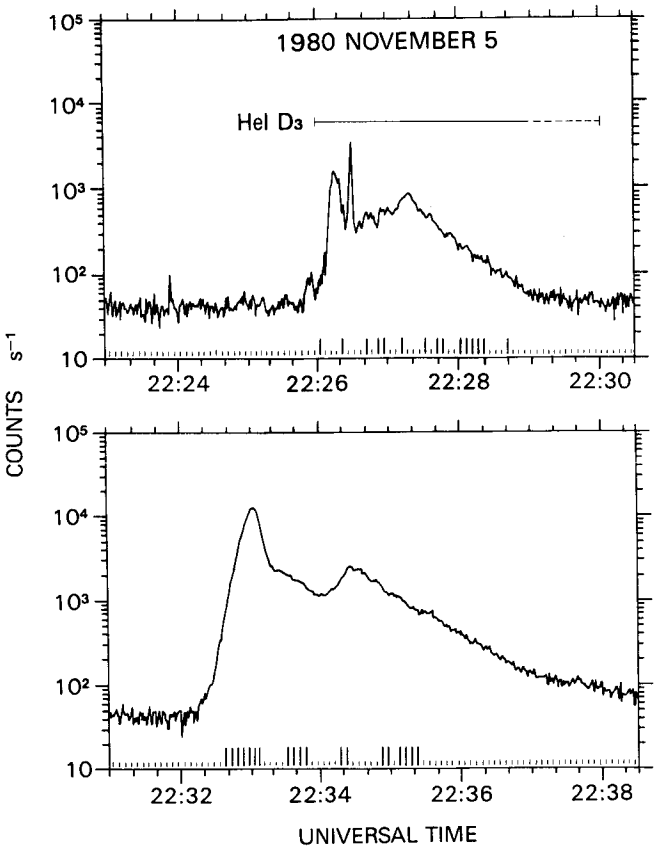

Figure 5A.14 The hard X-ray time profiles of the two flares on 1980 November 5 on a logarithmic scale with the times of the HeI D_3 observations also indicated. The short, evenly spaced, vertical lines just above the horizontal axis indicate when D_3 images were taken every 5 s on film at the Big Bear Solar Observatory. The longer vertical lines indicate the images which show obvious new or enhanced flare points in D_3. The entire impulsive phase is characterized by the presence of D_3 although not all new flare points are spatially resolved. The detection of these resolvable new points, however, is confirming evidence that energy is continuously released throughout the impulsive phase, not just during the rise.

terpreted as a small, low-lying loop with a strong horizontal field. From the optical data, Hoyng *et al.* concluded that the magnetic field rearranged itself over a small area in the center of the active region during the first flare and that a major rearrangement of the magnetic field took place during the second flare on a much larger spatial scale. During the final hard X-ray spike at 22:27:20 UT and on the decay of the first flare [Figure 5A.16(c)], the hard X-rays came almost exclusively from position T, although there is still a resolved bright point at lower energies from B.

At the onset of the second flare [Figure 5A.16(d)], the 16 to 22 keV X-rays came initially from region A and from a point to the south of B, at the position of the end of the bright Hα strand S1 seen in the first flare [Figure 5A.15(b)]. After the onset, the hard X-ray intensity continued the rapid rise and the bright points switched to position B and to a remote point at the eastern end of the filament [Figure 5A.17(a)]. Within 10 to 15 s, this remote emission had died away leaving a bright point at A [Figure 5A.16(e)]. During the final hard X-ray peak at 22:34:30 UT (Figure 5A.12), the hard X-rays were once more concentrated near T [Figure 5A.16(f)]. The appearance of the sequential hard X-ray brightenings from a number of distinct, and in one case widely separated, points suggests that there is a hierarchy of magnetic loops involved. The distant emission shown in Figure 5A.17(a), over 7×10^4 km away from the main flare site, is from the end of a structure which becomes completely filled with hot, X-ray emitting plasma during the decay of the flare [Figure 5A.17(b]. Bright points corresponding to A, T, and the initial hard X-ray bright point south of B are clearly resolved.

An estimate of the density of the soft-X-ray-emitting plasma is available during the decay of the second flare when FCS was operating in a spectral scanning mode. The measured Ne IX intercombination-to-forbidden-line ratio is density sensitive and indicates a maximum density of 1.5×10^{12} cm^{-3} at the time of the peak in the soft X-ray emission.

The Ca XIX and Fe XXV resonance line profiles observed with BCS during the impulsive phase of the second flare show broadening and extended blue wings visible for 30 s, beginning at the time of the peak hard X-ray flux. The blue shifts correspond to velocities between 200 and 500 km s^{-1}, and the line widths indicate that the turbulent velocities reached values of 100-200 km s^{-1}.

APPENDIX 5B. A REVIEW OF IMPULSIVE PHASE PHENOMENA

C. de Jager

5B.0 Introduction

In this appendix we present a brief review of impulsive phase phenomena in support of the models used in this chapter to compute the energies of the different components of the flares under study. A more complete review is given in Chapter 2 of this Workshop proceedings.

We begin with the observational characteristics of the impulsive phase, followed by the evidence for multi-thermal or non-thermal phenomena. The significance of time delays between hard X-rays and microwaves is discussed in terms of electron beams and Alfven waves, two-step acceleration, and secondary bursts at large distances from the primary source. Observations indicating the occurrence of chromo-